Deleterious effects of nonthermal electrons in shock ignition concept

Ph. Nicolaï,[1,*] J.-L. Feugeas,[1] M. Touati,[1] X. Ribeyre,[1] S. Gus'kov,[2] and V. Tikhonchuk[1]
[1]*Université Bordeaux-CNRS-CEA, Centre Laser Intense et Applications, UMR5107, 33405 Talence cedex, France*
[2]*P. N. Lebedev Physical Institute, RAS, Leninskii Prospect 53, Moscow 119991, Russia*
(Received 7 October 2013; published 25 March 2014)

Shock ignition concept is a promising approach to inertial confinement fusion that may allow obtaining high fusion energy gains with the existing laser technology. However, the spike driving laser intensities in the range of 1–10 PW/cm^2 produces the energetic electrons that may have a significant effect on the target performance. The hybrid numerical simulations including a radiation hydrodynamic code coupled to a rapid Fokker-Planck module are used to asses the role of hot electrons in the shock generation and the target preheat in the time scale of 100 ps and spatial scale of 100 μm. It is shown that depending on the electron energy distribution and the target density profile the hot electrons can either increase the shock amplitude or preheat the imploding shell. In particular, the exponential electron energy spectrum corresponding to the temperature of 30 keV in the present HiPER target design preheats the deuterium-tritium shell and jeopardizes its compression. Ways of improving the target performance are suggested.

DOI: 10.1103/PhysRevE.89.033107 PACS number(s): 52.50.Jm, 52.72.+v, 52.35.Tc, 98.38.Fs

I. INTRODUCTION

The transport and energy deposition of energetic electrons in laser-produced plasma are the major issues that directly impact the projects and studies related to inertial fusion for energy production. In laser-driven inertial fusion schemes a significant amount of energy can be transferred to nonthermal electrons, whatever the irradiation scheme used, direct shell irradiation [1] or indirect heating in a convertor cavity [2]. The energetic electrons can strongly modify the target performance and the fusion ignition conditions. The standard ignition schemes consider the interaction conditions where the hot electron generation is kept at a lowest possible level. However, this issue is of particular importance for the alternative ignition schemes called fast and shock ignition. In the fast ignition concept [3], a beam of relativistic electrons brings an energy necessary for creation of an ignition spot in the compressed part of the target. The MeV's energy electrons produced by an ultra-high laser intensity are launched at the target stagnation time, and although density reaches a few hundreds g/cc, the electrons travel up to the target core. The problems of angular divergence of such electron beams and their energy losses due to the collisions and self-generated or induced magnetic fields are still to be investigated [4]. The shock ignition (SI) scheme [5] relies on the high-intensity laser spike to excite a strong converging shock in the imploding dense shell. It is considered as the baseline for the European HiPER project for initial fusion energy [6,7]. The experiments [8,9] and the numerical simulations [10–12] show that a significant amount of nonthermal electrons can be produced in the SI conditions: at the laser intensities above 1 PW/cm^2 at the wavelength of 351 nm. These electrons induced by parametric instabilities such as stimulated Raman scattering and two-plasmon decay [13] have the effective temperature in the range of 30–70 keV. They may preheat the target, increasing its entropy, leading to a lower compression, detrimental for fuel combustion. However, the particularity of the SI scheme is that the spike is launched later in the implosion phase, when the shell areal density may be higher than the stopping range of electrons with the energies up to 100 keV [6,14–16].

This article is dedicated to the study of nonthermal electrons effects on the shock formation depending on the electron energy spectra and hydrodynamic density profiles. It is shown that the current SI target design [6] does not withstand the kinetic effects: the electrons generated at the shock launch time depose their energy through the imploding shell, which explodes thus preventing the target final compression. A possible way for improving target performance is proposed.

The article is structured as follows: in the next section the framework and the numerical tools used for this study are presented. In Sec. III the influence of the electron energy spectrum on shock formation is analyzed and illustrated with simplified setups. More realistic simulations and a way for improving target performance are presented in Sec. IV. The main results are summarized in Sec. V.

II. FRAMEWORK OF THE STUDY AND DEDICATED NUMERICAL TOOLS

The recent studies [17,18] of electron energy deposition in a dense plasma indicate that electrons stopped in the outer part of the shell can significantly boost the ignition shock in the SI conditions. The analytical results confirmed by the hybrid simulations show that an electron beam with the intensity 1 PW/cm^2 and the energy of 30 keV creates a shock wave with the amplitude about 300–400 Mbar in a solid DT block with the density of 10 g/cm^3. This is many times higher than the ablation pressure created by the laser beam of the same intensity. However, the demonstration of the principle of high-pressure generation in Refs. [17,18] has been limited to simplifying conditions of a monoenergetic electron beam and a steep density profile. Both effects are in fact very important for applications. A broad energy spectrum increases the depth of the energy deposition zone and consequently, the time of shock formation, while a finite areal mass of the payload may result in a less efficient shock formation or even in a shell

*nicolai@celia.u-bordeaux1.fr

explosion. In this article, the effects of a broad electron energy spectrum and smooth target density profile are analyzed.

The numerical tool used in this study is a combination of the two-dimensional axi-symmetric radiation hydrodynamic code CHIC [19] and a simplified Vlasov-Fokker-Planck code M1 [20–22]. The hydrocode is currently used to simulate laser-plasma interaction experiments [23,24]. It includes two-dimensional axially symmetric hydrodynamics with ion and classical or nonlocal electron heat conduction, thermal coupling of electrons and ions, and a detailed radiation transport. The opacity data are tabulated, assuming a local thermodynamic equilibrium (LTE) or a non-LTE depending on the plasma parameters. The radiative transport is computed assuming that the radiation field is quasistationary and weakly anisotropic (multigroup diffusion). The equations of state implemented in the code are based on a QEOS model [25] and SESAME [26] tables.

The kinetic code is based on the linearized kinetic equation for the fast electrons [27] reduced to two first angular moments of the distribution function f_e:

$$v^{-1}\partial_t \Psi_0 + \nabla \cdot \mathbf{\Psi}_1 = \partial_\epsilon (S_M \Psi_0 + e\,\mathbf{E}\cdot\mathbf{\Psi}_1), \tag{1}$$

$$\begin{aligned} v^{-1}\partial_t \mathbf{\Psi}_1 + \nabla \cdot \mathbf{\Psi}_2 &= \partial_\epsilon (S_M \mathbf{\Psi}_1 + e\,\mathbf{E}\cdot\mathbf{\Psi}_2) - k_1 \mathbf{\Psi}_1 \\ &\quad - (e/pv)\,\mathbf{E}\cdot(\Psi_0 \mathbf{I} - \mathbf{\Psi}_2) - (e/p)\,\mathbf{\Psi}_1 \times \mathbf{B}. \end{aligned} \tag{2}$$

Here $\Psi_0 = p^2 \int f_e\, d\mathbf{\Omega}$, $\mathbf{\Psi}_1 = p^2 \int \mathbf{\Omega}\, f_e\, d\mathbf{\Omega}$, and $\mathbf{\Psi}_2 = p^2 \int \mathbf{\Omega} \otimes \mathbf{\Omega}\, f_e\, d\mathbf{\Omega}$ are the angular moments, which are a scalar, a vector, and a tensor, respectively. The two first moments, Ψ_0 and $\mathbf{\Psi}_1$, are directly related to the electron density and energy and to the electron velocity and flux; $\mathbf{E}$ and $\mathbf{B}$ are the quasistatic electric and magnetic fields, p, v, and ϵ are the particle momentum, velocity, and energy, and $\mathbf{\Omega} = \mathbf{p}/p$ is its propagation direction. The function $S_M(\epsilon)$ is the electron collisional stopping power, and $k_1(\epsilon)$ is the coefficient characterizing the electron scattering on ions. The right-hand side of Eq. (1) can be interpreted as the stopping power due to the collisions and the electric field yielding the background plasma heating. The terms with the electric and magnetic fields appearing in Eq. (2) account for the electron acceleration, slowing down, and deflexion.

The M1 model is different from the Legendre polynomial expansion [28] by the closure relation. Using the entropy maximization under the constraint of the first moment construction, the second angular moment $\mathbf{\Psi}_2$ is expressed as a function of the first two moments Ψ_0 and $\mathbf{\Psi}_1$ [20]. Contrary to the Legendre polynomial expansion P1 [27], the M1 model describes also a strongly anisotropic electron distributions, while maintaining the whole distribution function always positive. This model assumes that nonthermal electrons interact with the electron and ion background but not themselves. That supposes a low density of nonthermal electrons relatively to the plasma density. Moreover, the M1 model does not compute the laser plasma interaction. The source of hot electrons in the plasma corona is characterized by the energy distribution according to particle in cell code results or to the scaling laws [29,30], an angular distribution and a temporal dependence. At every time step, the M1 module uses hydrodynamic profiles computed by the CHIC code and the electric and magnetic fields calculated according to the generalized Ohm's law. The M1 module computes the electron transport, the energy deposition, and the self-consistent electric field that, in turn, contribute to the evolution equations of the plasma electron temperature and the magnetic field.

III. ELECTRON ENERGY SPECTRUM EFFECTS

We consider first a simplified geometry of a 100 μm long DT plasma with sharp boundaries. The initial temperature is 1 eV, and the density of 10 g/cm^3 corresponds to the HiPER target implosion at the ignition shock launch time of 10.2 ns [6,7]. Figure 1 compares the pressure, density, and temperature profiles for cases of 30 and 100 keV monoenergetic electron beams and a beam with the 30 keV temperature. For all cases, the electron beam intensity equals 1 PW/cm^2. The electrons are coming from the left. The DT target is initially set between 0 and 100 μm.

For such a simplified density profile, an electron beam with a kinetic energy of 30 keV and an intensity of 1 PW/cm^2 could produce a shock wave with a pressure of 380 Mbar within a very short time of 20 ps [17]. These values are consistent with the analytical model [18] that provides the expressions for the maximum pressure and the time when it is achieved: $P = (6\pi)^{-1/3} I^{2/3} \rho^{1/3}$ and $t_m = (9/2\pi)^{1/3} X(\varepsilon^2)(\rho/I)^{1/3}$. Here I, ρ, X, and ε are intensity, density, stopping length, and electron energy. In our conditions, that corresponds to $P \simeq 380$ Mb and $t_m \simeq 20$ ps. Due to a short stopping length, X (30 keV) $\simeq$ 1.8 μm, the temperature profiles shown in Fig. 1(c) present characteristics of a surface heating with associated high values, above 1 keV after 300 ps. This first test case shows a possible beneficial effect for SI of the energetic electrons induced by parametric instabilities. However, it is important to consider the role of energy distribution in the electron beam. As the electron beam stopping power is proportional to the square of electron energy, the depth of energy deposition of a broadband beam increases with the beam width thus delaying the time of shock formation.

The electron energies in the two following examples are chosen in such a way that the depths of beam energy deposition are approximately the same, about 15–20 μm. The maximum of energy deposition in the monoenergetic 100 keV electron beam case is 15 μm inside the DT block. This can be seen, in Fig. 1(f), in a characteristic temperature shape, which has a maximum inside the plasma with the temperature reaching 100 eV after 200 ps. Likewise, a depletion induced by the temperature increase is clearly visible in density profiles, as shown in Fig. 1(e). This depletion is associated to a shock formation and its propagation through the DT block. In the same time, due to the plasma heating, a rarefaction wave propagates inside from the plasma boundary. Contrary to the case of monoenergetic 30 keV electrons, due to a longer electron mean-free path, the pressure loading time is much longer, about 150–200 ps, in Fig. 1(d). It rises to the maximum of 410–450 Mbar, which is slightly higher than in the 30 keV monoenergetic electron beam, and it is 5 times higher than the pressure induced by a laser beam with the same intensity. The maximum density compression of 2.8 times the initial density is obtained with even a longer delay of about 300 ps; see

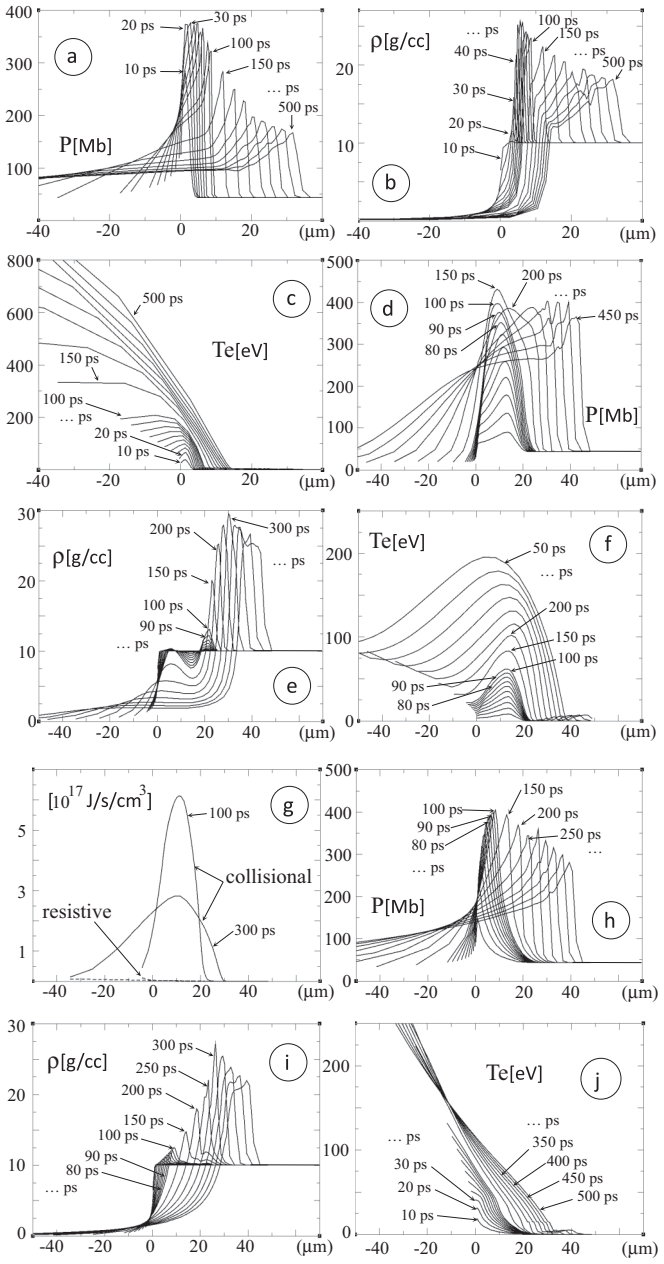

FIG. 1. Pressure (a), density (b), and temperature (c) profiles every 10 ps up to 100 ps and every 50 ps after, for the case of a monoenergetic 30 keV electron beam. Pressure (d), density (e), temperature (f), and energy deposition (g) profiles with the same delays for the case of a monoenergetic 100 keV electron beam. Pressure (h), density (i), and temperature (j) profiles for the case of an exponential electron energy distribution with the 30 keV temperature.

Fig. 1(e). Under these conditions, the electrons mainly loose their energy in electron-electron collisions in a high-density DT plasma. As shown in Fig. 1(g), the resistive effects are negligible.

The case with the exponential electron energy distribution demonstrates an almost identical process of the shock formation. The difference is in the maximum of energy deposition, which is at the plasma edge. Consequently the temperature profiles correspond to the surfacic heating rather than the volumic one. Nevertheless, the maximum pressure and density compression times, about 100 ps and 300 ps, respectively, are close to the case of a monoenergetic 100 keV electron beam. This indicates the importance of energetic electrons, about 100 keV, in the 30 keV temperature spectrum. These two examples show that the 100 keV electrons have no detrimental effect on the shock amplitude. The intense beams of energetic electrons can create rather high shock wave pressures that are interesting for inertial fusion and the studies of the equation of state. However, in application to the SI scheme, the delay with the shock launch time needs to be accounted for, otherwise the additional boost of the central hot spot may arrive too late.

IV. DENSITY PROFILE EFFECTS

The target density profile has also an important effect on the shock formation. In a more realistic case corresponding to the target designed for the HiPER project [6,7] the areal densities of the ablated plasma and the compressed shell are comparable with the electron stopping range. Figure 2 presents the density profile of the HiPER target at the moment of the igniting shock launch of 10.2 ns. The areal mass of the low density part is of a few mg/cm^2, and the compressed shell is ∼23 mg/cm^2. These numbers are comparable to the electron beam range of ∼20 mg/cm^2 found in the cases presented in Fig. 1.

The shock formation dynamics presented in Fig. 2. In the case of a monoenergetic 30 keV electron beam presented in panels b–d, the electron range ∼2 mg/cm^2 is comparable with the corona thickness. Then the electrons do not reach the dense shell, depositing the major part of their energy in a plasma with the density about 0.1–0.2 g/cm^3, shown in Fig. 2(d). The pressure increase occurs in front of the dense part and compresses it. Although the pressure reaches 350 Mbar inducing the density maximum of 17 g/cm^3, the shock is rather weak. The times required to reach maxima of pressure and density are, respectively, 150 ps and 250 ps, leading to the same problem for the target performance.

The situation is different for the case of a 100 keV monoenergetic electron beam shown in Fig. 2(e)–2(g). The electrons are depositing their energy in front of but also in the compressed part of the shell. The pressure increases up to 330 Mbar but into the density bump. No compression further is possible and the shell expands. Thus, a homogeneous energy deposition across the shell in this situation leads to the formation of a rarefaction wave. This is rather similar to the exploding pusher scheme considered in the early days of inertial fusion studies [31,32].

The case of an exponential electron spectrum with the 30 keV temperature is shown in Fig. 2(h)–2(j). Similarly to the previous case, the pressure increases up to 120 Mbar without producing any significant compression. The electron energy is deposited in the front of the dense shell, but also partly inside it. In addition, the pressure-driven shock formation takes too long time compared to the decompression induced by electron heating. Then, instead of a shock, the rarefaction wave is formed. Thus, the areal density of the HiPER target at the moment of the spike launch is not sufficient for the shock formation. There is no positive effect of the fast electrons with the energies in the range of 30–100 keV on the compression. Worse, they are preheating shell almost

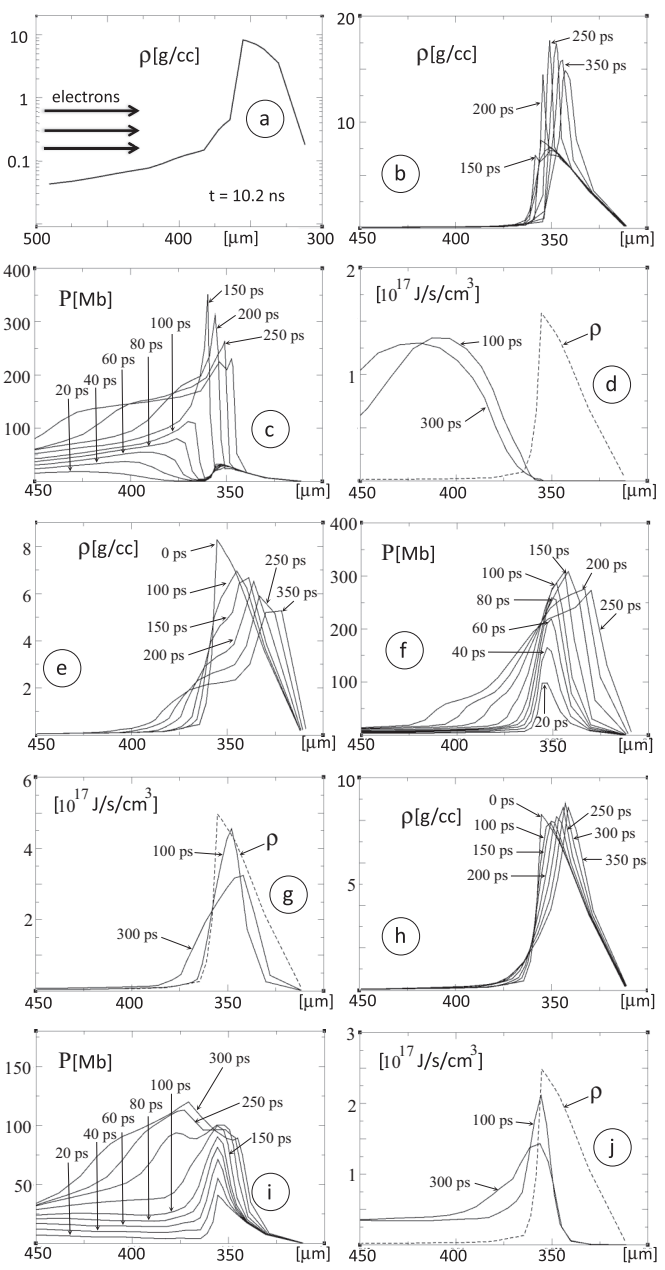

FIG. 2. Realistic target density profile at the shock launching time, 10.2 ns (a). The electrons are coming from the left. Density (b), pressure (c), and energy deposition (d) profiles for the case of a monoenergetic 30 keV electron beam. Density (e), pressure (f), and energy deposition (g) profiles for the case of a monoenergetic 100 keV electron beam. Density (h), pressure (i), and energy deposition (j) profiles for the case of an exponential electron energy distribution with the 30 keV temperature.

homogeneously, jeopardizing its compression or provoking its explosion.

These examples do not question the general idea of SI scheme but rather indicate the necessity of a new target design more resistant to the hot electron preheating. In order to improve the performance, the SI target must be modified. Its initial mass may be increased or the shock launch time delayed to give more time to the target to enhance its areal

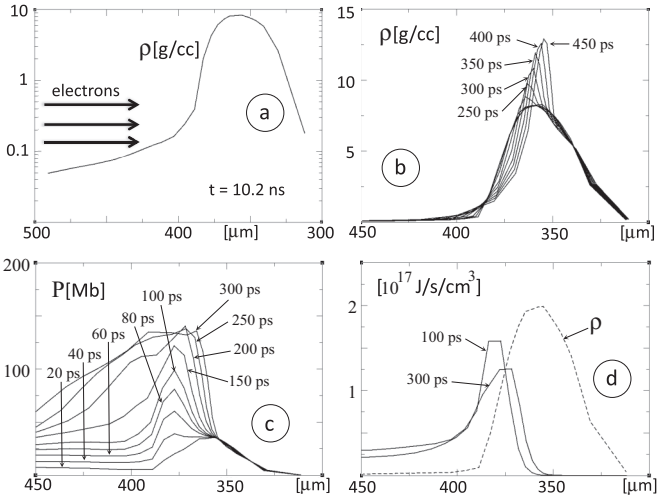

FIG. 3. Target density profile (a). Density (b), pressure (c), and energy deposition (d) profiles for the case of an exponential electron energy distribution with the 30 keV temperature.

density. But in the latter case, shock formation time needs to be compatible with the stagnation time. To verify the electron preheat reduction due to the areal density enhancement, we increased the shell areal density by 50% to $\simeq$37 mg/cm^2. The density profile is presented in Fig. 3 for the case of an electron beam with a 30 keV exponential spectrum. Although the electrons penetrate partly into the dense shell, Fig. 3(d) shows that the energy is deposited before the density maximum. A large part of the shell is not directly affected by nonthermal electrons. The pressure in Fig. 3(c) does not grow to greater values than previously, but because a part of the target remains cold, it can be compressed. This compression can be further optimized by adjusting the plasma density profile and the electron energy distribution.

V. CONCLUSION

Whatever the energy spectrum of fast electrons, in order to produce a very high pressure of hundreds of Mbar, the target density profile needs to be specially shaped. The electron mean-free path should be much shorter than the dense shell thickness. The areal density of the target at the shock launching time has to be significantly greater than the electron range in order to avoid the shell preheat. Whether this condition is not respected, preheating induces the target decompression or at least prevents the target compression. Moreover, the depth of the energy deposition for a 30 keV temperature spectrum is much larger that the one of a 30 keV energetic electron. It has been shown in this work that the suprathermal electrons, about 100 keV, strongly contribute to the target heating and shock formation. In addition, the time required for reaching the maximum pressure increases with the electron mean-free path. The 100 keV electrons could induce too long of a shock formation time; even this does not directly affect the target performance, it does not contribute to the enhancement of the laser-driven shock anymore. Based on present simulation results, we conclude that the DT-HIPER target [6,7] is not suited for shock ignition. A target areal density increase may

improve target performance by reducing preheating effects. The optimization should be twofold to enhance pressure due to nonthermal electrons but also to limit their influence on the target preheat. The areal density modification could be directly done by changing the initial target mass or by delaying slightly the shock launching time. For example, a 200 ps laser spike delay yields the acceptable areal density. These changes are implying also modifications of the implosion velocity and shock timing and may lead to a lower energy gains.

The present examples are limited to the electron beam power of 1 PW/cm^2. Assuming the laser intensity of 5–7 PW/cm^2, which corresponds to the conversion efficiency to electrons of about 15–20%, the exponential 30 keV electron energy spectrum is also consistent with the existing experimental and simulation data [9,12]. Our conclusions will not be modified by a different energy spectrum as long as the electron mean-free path remains the same. Moreover, the thermal electron transport does not influence results of this study. Indeed, the heat-carrying electrons have a velocity $\sim 2.6\ v_{th}$ where v_{th} is the thermal velocity. Above an intensity of 10^{15} W/cm^2, the heat flux becomes nonlocal and the characteristic velocity decreases to $\sim 2.1\ v_{th}$ as shown in Refs. [33,34]. The equivalent heat-carrying electron temperature is less than the 30 keV temperature of hot electrons used in this study. The corresponding mean-free path is smaller, and these electrons do not modify the preheat induced by the nonthermal electrons produced by parametric instabilities. Finally, the multidimensional effects such as the lateral expansion and losses or self-generated magnetic fields need to be considered. However, in the existent SI designs, the laser spike has a spherical symmetry, and one-dimensional simulations are representative.

ACKNOWLEDGMENTS

This work is supported partly by the EURATOM within the Keep-in-Touch activities, the Aquitaine Regional Council, the Russian Foundation for Basic Research (project No. 12-02-92101-JF), and the European program LASERLAB.

[1] S. Atzeni and J. Meyer-ter-Vehn, *The Physics of Inertial Fusion* (Oxford University Press, Oxford, 2004).
[2] J. D. Lindl, P. Amendt, R. L. Berger, S. G. Glendinning, S. H. Glenzer, S. W. Haan, R. L. Kauffman, O. L. Landen, and L. J. Suter, Phys. Plasmas **11**, 339 (2004).
[3] M. Tabak, J. Hammer, M. E. Glinsky, W. L. Kruer, S. C. Wilks, J. Woodworth, E. M. Campbell, M. D. Perry, and R. J. Mason, Phys. Plasmas **1**, 1626 (1994).
[4] B. Vauzour, J. J. Santos, A. Debayle, S. Hulin, H.-P. Schlenvoigt, X. Vaisseau, D. Batani, S. D. Baton, J. J. Honrubia, Ph. Nicolaï, F. N. Beg, R. Benocci, S. Chawla, M. Coury, F. Dorchies, C. Fourment, E. d'Humières, L. C. Jarrot, P. McKenna, Y. J. Rhee, V. T. Tikhonchuk, L. Volpe, and V. Yahia, Phys. Rev. Lett. **109**, 255002 (2012).
[5] R. Betti, C. D. Zhou, K. S. Anderson, J. L. Perkins, W. Theobald, and A. A. Solodov, Phys. Rev. Lett. **98**, 155001 (2007).
[6] X. Ribeyre, G. Schurtz, M. Lafon, S. Galera, and S. Weber, Plasma Phys. Control. Fusion **51**, 015013 (2009).
[7] S. Atzeni, J. R. Davies, L. Hallo, J. J. Honrubia, P.-H. Maire, M. Olazabal-Loumé, J.-L. Feugeas, X. Ribeyre, A. Schiavi, G. Schurtz, J. Breil, Ph. Nicolaï, Nucl. Fusion **49**, 055008 (2009).
[8] V. A. Smalyuk, D. Shvarts, R. Betti, J. A. Delettrez, D. H. Edgell, V. Yu. Glebov, V. N. Goncharov, R. L. McCrory, D. D. Meyerhofer, P. B. Radha, S. P. Regan, T. C. Sangster, W. Seka, S. Skupsky, C. Stoeckl, B. Yaakobi, J. A. Frenje, C. K. Li, R. D. Petrasso, and F. H. Séguin, Phys. Rev. Lett. **100**, 185005 (2008).
[9] W. Theobald, R. Nora, M. Lafon, A. Casner, X. Ribeyre, K. S. Anderson, R. Betti, J. A. Delettrez, J. A. Frenje, V. Yu. Glebov, O. V. Gotchev, M. Hohenberger, S. X. Hu, F. J. Marshall, D. D. Meyerhofer, T. C. Sangster, G. Schurtz, W. Seka, V. A. Smalyuk, C. Stoeckl, and B. Yaakobi, Phys. Plasmas **19**, 102706 (2012).
[10] O. Klimo, S. Weber, V. T. Tikhonchuk, and J. Limpouch, Plasma Phys. Control. Fusion **52**, 055013 (2010).
[11] O. Klimo, V. T. Tikhonchuk, X. Ribeyre, G. Schurtz, C. Riconda, S. Weber, and J. Limpouch, Phys. Plasmas **18**, 082709 (2011).
[12] S. Weber, C. Riconda, O. Klimo, A. Héron, and V. T. Tikhonchuk, Phys. Rev. E **85**, 016403 (2012).
[13] W. Kruer, *The Physics of Laser Plasma Interactions* (Addison-Wesley, New York, 1988).
[14] R. Betti, W. Theobald, C. D. Zhou, K. S. Anderson, P. W. McKenty, S. Skupsky, D. Shvarts, V. N. Goncharov, J. A. Delettrez, P. B. Radha, T. C. Sangster, C. Stoeckl, and D. D. Meyerhofer, J. Phys. Conf. Ser. **112**, 022024 (2008).
[15] L. J. Perkins, R. Betti, K. N. LaFortune, and W. H. Williams, Phys. Rev. Lett. **103**, 045004 (2009).
[16] M. Terry, L. Perkins and S. Speke, Phys. Plasmas **19**, 112705 (2012).
[17] S. Gus'kov, X. Ribeyre, M. Touati, J.-L. Feugeas, Ph. Nicolaï, V. Tikhonchuk, Phys. Rev. Lett. **109**, 255004 (2012).
[18] X. Ribeyre, S. Gus'kov, J.-L. Feugeas, Ph. Nicolaï, and V. T. Tikhonchuk, Phys. Plasmas **20**, 062705 (2013).
[19] J. Breil and P.-H. Maire, J. Comput. Phys. **224**, 785 (2007).
[20] B. Dubroca, J.-L. Feugeas, and M. Frank, European Phys. J. D **60**, 301 (2010).
[21] Ph. Nicolaï, J.-L. Feugeas, C. Regan, M. Olazabal-Loumé, J. Breil, B. Dubroca, J.-P. Morreeuw, and V. Tikhonchuk, Phys. Rev. E **84**, 016402 (2011).
[22] R. H. H. Scott, C. Beaucourt, H.-P. Schlenvoigt, K. Markey, K. L. Lancaster, C. P. Ridgers, C. M. Brenner, J. Pasley, R. J. Gray, I. O. Musgrave, A. P. L. Robinson, K. Li, M. M. Notley, J. R. Davies, S. D. Baton, J. J. Santos, J.-L. Feugeas, Ph. Nicolaï, G. Malka, V. T. Tikhonchuk, P. McKenna, D. Neely, S. J. Rose, and P. A. Norreys, Phys. Rev. Lett. **109**, 015001 (2012).
[23] F. Perez *et al.*, Phys. Rev. Lett. **107**, 065004 (2011).
[24] B. Vauzour *et al.*, Phys. Plasmas **18**, 043108 (2011).
[25] R. More, K. Warren, D. Young, and G. Zimmerman, Phys. Fluids **31**, 3059 (1988).
[26] See SESAME Report on Los Alamos Equation-of-State Library, LANL Report No. (T4 Group LANL, Los Alamos, 1983).

[27] I. Shkarofsky, T. Johnston, and M. Bachynskii, *The Particle Kinetics of Plasmas* (Addison-Wesley, Reading, MA 1966).
[28] J. P. Matte and J. Virmont, Phys. Rev. Lett. **49**, 1936 (1982).
[29] F. N. Beg, A. R. Bell, A. E. Dangor, C. N. Danson, A. P. Fews, M. E. Glinsky, B. A. Hammel, P. Lee, P. A. Norreys, and M. Tatarakis, Phys. Plasmas **4**, 447 (1997).
[30] S. Wilks and W. Kruer, IEEE J. Quantum Electronics **33**, 1954 (1997).
[31] M. D. Rosen and J. H. Nuckolls, Phys. Fluids **22**, 1393 (1979).
[32] B. Alhorn and M. H. Key, Plasma Phys. **23**, 435 (1981).
[33] E. Epperlein and R. Short, Phys. Fluids B **29**, 1029 (1986).
[34] Ph. Nicolaï, J.-L. Feugeas, and G. Schurtz, Phys. Plasmas **13**, 032701 (2006).